communications earth & environment

Article

https://doi.org/10.1038/s43247-024-01863-0

Central European warm phases recorded by episodic speleothem growth during MIS 3

Check for updates

Jennifer Klose ✉, Michael Weber & Denis Scholz

Speleothems provide exceptional age control and are a valuable archive for the identification of warm phases in temperate climates. Here we present a speleothem composite record from Germany, which shows episodic growth during the last glacial period, coinciding with several Greenland Interstadials. Using a combined approach of high-resolution solution and in-situ laser ablation ^{230}Th/U-dating, we were able to precisely constrain the timing and duration of several particularly warm phases during Marine Isotope Stage 3. Climatic conditions favourable for speleothem growth occurred episodically until 32,000 years ago, much longer than reported from existing speleothem records. The inception of speleothem growth lags the onset of Greenland Interstadials and covers approximately 88% of their total duration during early, and approximately 25% during middle and late Marine Isotope Stage 3. This indicates progressive climatic cooling during Marine Isotope Stage 3, with the speleothem growth phases representing persistent Central European warm phases.

The last glacial period and especially Marine Isotope Stage (MIS) 3 was characterised by several events of abrupt climate change known as Dansgaard-Oeschger (DO) events[1–3], resulting in re-occurring warm Greenland Interstadials (GI) and cold Greenland Stadials (GS). The DO events are visible as rapid shifts in the $\delta^{18}O$ and $\delta^{15}N$ values of Greenland ice cores[3] reflecting regional temperature increases of up to 16 °C (± 3 °C)[4], coinciding with almost a doubling of the local snow accumulation[5] and rapid changes in aerosol concentrations[6]. These shifts towards warmer conditions often occurred within only a few decades[1,4,7]. The DO events have been linked with rapid changes in ocean and atmospheric circulation in the North Atlantic region[1,8–14] and were associated with a reduction and retraction of North Atlantic sea ice, a strong Atlantic Meridional Overturning Circulation (AMOC) and a reduced influence of Antarctic Bottom Water (AABW)[15]. However, their main trigger still remains a topic of debate[16–18].

The DO events show a supra-regional character with sites ranging from the North Atlantic to Asia as well as monsoon regions in the southern hemisphere[6,19–22], and have been identified in numerous climate archives, such as ocean sediment cores from the Atlantic[23–26] and terrestrial records from monsoon regions[27,28]. These records indicate that the timing of climate change was synchronous in the North Atlantic, the Asian, and South American Monsoon regions[18] as well as in the low to mid-latitudes[22,29].

Due to the usually short duration and rapid onset of the DO events, the determination of their precise timing remains challenging. For the Greenland ice cores, the commonly used GICC05 time scale[30], which was constructed by counting continuously accumulating annual layers, the accumulative counting errors progressively increase from 0.8 ka (at ~28 ka BP) to 2.5 ka (at ~60 ka BP)[3,30]. This uncertainty hampers the cross-dating and general comparability with other records, including the identification of potential leads and lags between regions and climate subsystems. This is further complicated by the low temporal resolution and dating accuracy achievable in many climate archives. Speleothems offer the exceptional possibility to establish precise and accurate independent age models based on U-series dating[31,32]. Corrick et al.[18] compiled 63 published speleothem records from the European Mediterranean region, the Asian Summer Monsoon region, and the South American Monsoon realm, constructed a Speleothem Interstadial Onset Compilation data set (SIOC19) and compared it with the GICC05 chronology of GI onsets. The SIOC19 chronology does not include any speleothems from Central Europe. Most MIS 3 speleothem records from Europe stem from the Alps, where liquid water underneath temperate glaciers and pyrite oxidation allowed for speleothem growth even in case of absence of soil cover[21,33]. Additional speleothem records from MIS 3 come from caves located in southwestern Europe[34,35]. So far, the northernmost speleothem MIS 3 proxy record from Central Europe is from Bunker Cave, western Germany (49°N, 7°E, Fig. S1), where two relatively short growth phases during MIS 3 have been identified[36].

Located in close vicinity to and downwind of Greenland and the North Atlantic, Central Europe is highly susceptible to climatic perturbations in higher latitudes, and the influence of the DO events has been recorded in other palaeoclimate archives from the region[37,38]. However, it has proven

Institute for Geosciences, Johannes Gutenberg University, Mainz, Germany. ✉e-mail: jeklose@uni-mainz.de

challenging to constrain the precise timing of the DO events in Central Europe due to the lack of independently dated records (i.e., not tuned to GICC05). The lack of speleothem records from Central Europe during MIS 3 may have numerous reasons, including flooding or infilling of cave passages, drought, permafrost conditions, or a general lack of vegetation above the cave. To enable speleothem growth, liquid water, as well as soil and vegetation cover, are required, which may not have been continuously available during MIS 3 due to the cold and dry periglacial climate[39].

Ground temperature thus is a key factor for speleothem growth, which when falling below zero for more than two consecutive years initiates permafrost conditions[40,41]. The extent of periglacial periods and (continuous) permafrost conditions during MIS 3, as for instance documented by the occurrence of cryogenic cave calcites in Central Europe[42], is, however, both spatially and temporally poorly constrained. It is also uncertain whether the (short) warming during the DO events was able to initiate sufficient permafrost thaw to allow active infiltration and speleothem deposition. These questions highlight the need for precisely and absolutely dated last glacial climate records from Central Europe.

Here we present three exceptionally precisely dated speleothems from Bleßberg Cave, Central Germany, which show several distinctively separated growth phases during MIS 3. These growth phases coincide with GIs, but do not cover entire DO cycles. The flowstone samples are characterised by small, episodic growth phases resulting in complex growth characteristics on the µm-scale. Therefore, we applied a variety of sampling approaches, including in-situ dating techniques.

Results and Discussion

Timing and duration of growth phases

Three flowstones (BB-9, BB-10, and BB-15) were retrieved from Bleßberg Cave, Central Germany (Fig. S1, ca. 500 m above sea level, 50°25'28" N and 11°01'13" E, see supplement for details). All flowstones are composed of calcite and show distinct growth intervals, interrupted by episodes of deposition of detrital material. ^{230}Th/U-dating reveals that speleothem growth occurred episodically during MIS 3 when environmental conditions were favourable (Tables S1a – f and S2). The uppermost parts of all samples grew during the Late Glacial and early Holocene, which is not part of this study. All three samples grew discontinuously between 60 and 33 ka BP. BB-10 and BB-15 (Fig. S2) more prominently cover the earlier phases of MIS 3 between ca. 60 and 50 ka BP and show only sporadic growth in the later phases of MIS 3 (ca. 39–33 ka BP). BB-9 covers a longer, but strongly intermittent period during the middle and late part of MIS 3 (ca. 47–33 ka BP), with shorter growth phases interrupted by many growth stops (hiatuses) (Fig. S3).

The episodic growth pattern of the samples is characterised by alternating bright (continuous growth phases) and dark (hiatuses) sections. Some of the bright sections—especially of sample BB-9—only have a thickness of 0.6–2 mm (Fig. 1). The hiatuses are often associated with detrital material, such as clay, deposited during periods without speleothem growth. These periods coincide with phases of colder climate, and we interpret them as growth stops forced by climatic changes and limited water availability inside the cave. Since Th preferably sticks to clay minerals, the hiatuses show elevated Th concentrations. The ^{230}Th/U-dating method relies on the decay of ^{238}U and ^{234}U to ^{230}Th, with the assumption of the absence of initial ^{230}Th[31]. Due to the high content of detrital Th, this assumption is violated for the hiatuses and can result in apparently too old ages close to the growth stops. Accurate ^{230}Th/U-dating of these sections is thus challenging and requires precise determination of the spatial extent of the detrital layers to avoid detrital contamination of the samples.

Macro- or microscopic assessment of the spatial extent of the detrital layers is difficult due to their spatially heterogeneous character (Fig. 1a – c). The detrital content of speleothem calcite is also reflected by elevated concentrations of specific trace elements (such as Th or Al). We determined trace elements by applying conventional line scan analysis for samples BB-9 and −10 as well as trace element mapping for sample BB-9 (Fig. 1a – c). The line scan data were used for a principal component analysis (PCA), with the first principal component (PC1) representing the elements related to detrital contamination (Fig. 1a). PC1 was then used to precisely constrain the spatial extent of the detrital layers (grey bars in Fig. 1). The trace element maps also show the spatial heterogeneity of the layers (Fig. 1b and c), especially in close vicinity to the hiatuses. Based on these data, we used a combination of different approaches for the sampling and ^{230}Th/U-dating (handheld drilling, micromilling, and laser ablation (LA)) to avoid contaminated areas. Samples obtained by handheld drilling or micromilling will further be referred to as solution ^{230}Th/U-ages.

For the solution ^{230}Th/U-ages, sampling of detrital material often could not be avoided. This is reflected by low (^{230}Th/^{232}Th) activity ratios (Table S1a – f) and results in increased age uncertainties due to the correction for detrital contamination, which is conventionally applied to all ^{230}Th/U-ages. To construct a reliable age model using conventional age-depth models, at least three precise ^{230}Th/U-ages for each growth phase are required. However, in many cases, only 1−2 high-precision solution ages per growth phase could be obtained, in particular for very thin growth sections. Therefore, we performed high-spatial-resolution LA ^{230}Th/U-dating along the growth layers (Fig. S3b) on samples BB-9 and −10. In addition, we measured continuous LA ^{230}Th/U-dating line scans perpendicularly to the growth layers (Fig. S3c) on all three samples. The latter was then used to calculate further ^{230}Th/U-ages based on the obtained data (Fig. 1h and i, see methods for details). These individual LA line scan ^{230}Th/U-ages were calculated at 0.2 mm resolution and represent a mean ^{230}Th/U-age of the corresponding material. This combination of some very precise solution ^{230}Th/U-ages (age uncertainties ≤ 0.4%) and a large number of LA ^{230}Th/U ages with larger uncertainty (~ 5–10%) but very high spatial resolution (0.2 mm) enables us to calculate age models for all growth phases of the three flowstone samples. In total, 566 ^{230}Th/U-ages (BB-9: solution n = 22, LA n = 101; BB-10 solution n = 13, LA n = 259; BB-15 solution n = 8, LA n = 163) were determined and used for age modelling.

The high-resolution LA ^{230}Th/U-data also provide detailed information about the distribution of U and Th across the samples. The concentration of ^{232}Th is an indicator of detrital contamination, whereas high (^{232}Th/^{238}U) and low (^{230}Th/^{232}Th) ratios reflect a high degree of contamination. This is the case around and within the hiatuses (Fig. 1e and f), and the corresponding LA ^{230}Th/U-ages are apparently too old (Fig. 1d). These data support our observations based on the trace element data. Initial (^{234}U/^{238}U) activity ratios, $(^{234}U/^{238}U)_i$, also show distinct changes around the hiatuses (Fig. 1h), and can thus also be used as an indicator for growth stops, even if they do not coincide with a visible detrital layer. Based on this observation, we identified two further growth stops in apparently continuous growth phases of samples BB-10 and −15. These are also reflected by apparently too-old LA ^{230}Th/U-ages (Fig. S4).

The age models for all three samples were calculated using a section-wise linear fit based on a Monte-Carlo simulation with 10,000 iterations (Fig. 2a and b, see methods for details), which weights precise ages more strongly and does not only provide the age-depth model and its 95% confidence intervals, but also a distribution of all calculated ages (Figs. 2c, d and 3d – f). This distribution is shown as a histogram to visualise the probability of the age ranges of the individual growth phases (see Fig. S5 for details). To allow comparison between the growth phases, the number of bins for the histograms was set to 20 for all growth phases (Fig. 3). Therefore, the width of the individual bins and the histogram reflect the precision of the age model for the individual growth phases. Even for sample BB-9, which proved to be the most challenging sample due to the very thin growth layers, we obtained precise age models for the majority of the individual growth phases (Fig. 3d). This highlights the great potential of our dating approach for flowstone samples with particularly thin growth layers, which are often considered as less suitable climate archives due to their episodic growth pattern. Unfortunately, in a few cases, even our approach resulted in relatively imprecise age models, and a clear assignment to a single GI was not possible. The reason for the lower precision of the corresponding age models is a lack of precise solution ages, either due to unavoidable detrital contamination (e.g., growth phase 4 of BB-9 or growth phase 3 of BB-15) or due

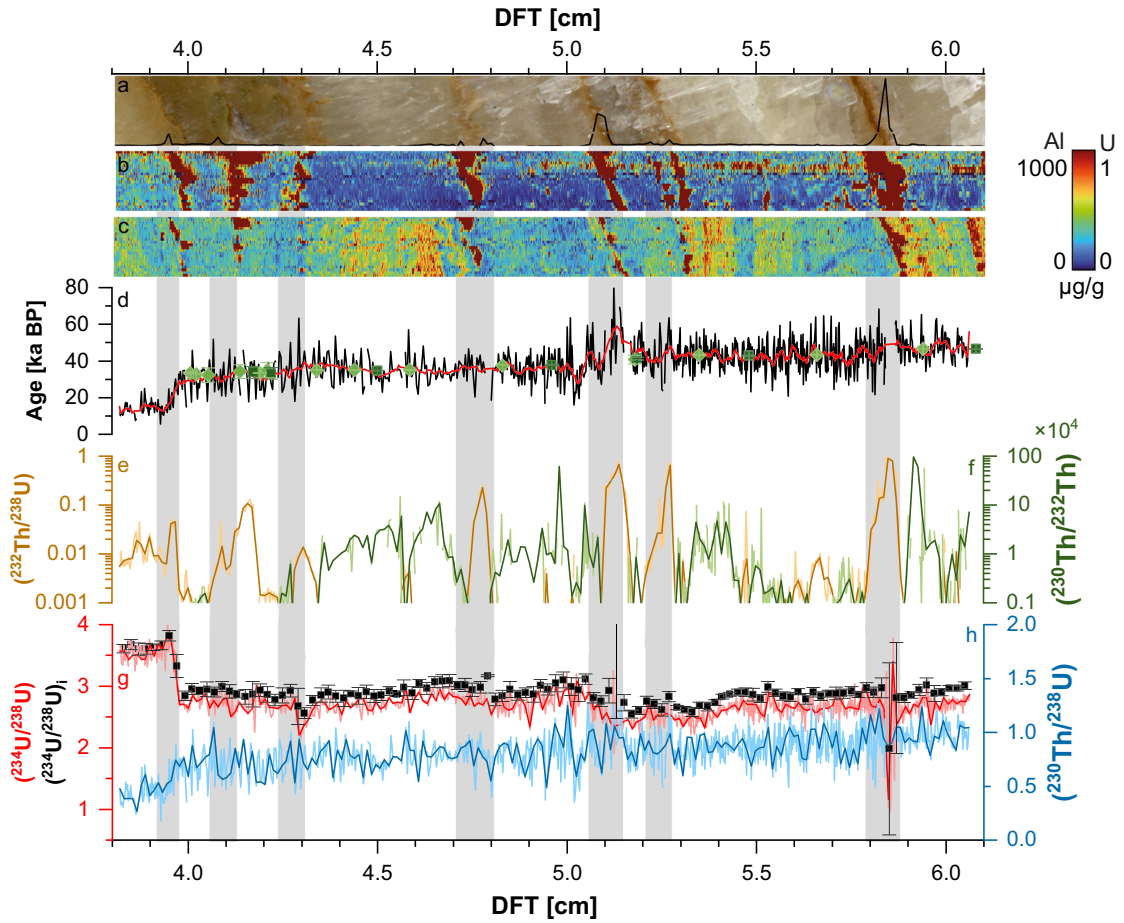

Fig. 1 | Overview of measurements applied to sample BB-9. Grey bars indicate the defined spatial extent of the hiatuses. **a** detrital component of the trace element principal component analysis (black line) on a scan of the sample showing the area of the trace element concentration mapping of Al (**b**) and U (**c**). **d** shows corrected ^{230}Th/U-ages obtained by laser ablation line scan analyses in high resolution (black) and smoothed by a 10 pt Adjacent-Averaging (red). Solution ages are given as light green diamonds (micromilling) and dark green squares (handheld drill). **e** and **f** indicate the degree of detrital contamination within the sample obtained by laser ablation, both axes are on a logarithmic scale. **g** and **h** show the laser ablation line scan data of (^{234}U/^{238}U) (red) and (^{230}Th/^{238}U) (blue), which were used to calculate the ages in **d**, the black dots indicate $(^{234}U/^{238}U)_i$ at 0.2 mm resolution.

to a lower spatial resolution in case of longer growth phases (e.g., growth phase 1.3 of sample BB-10). Thus, our dating approach works best with a few high-precision solution ages that can be used as anchor points for the high-resolution LA ^{230}Th/U-ages with larger age uncertainties.

Speleothem growth requires both liquid water and a vegetation cover above the cave. These requirements were fulfilled for some time intervals during MIS 3 in Central Europe, as demonstrated by the formation of speleothems in Bleßberg cave (Fig. 3). However, these growth phases were frequently interrupted, when environmental conditions inhibited speleothem formation during cold stadial periods. Permafrost conditions in Central Europe can explain the absence of speleothem formation. Cryogenic cave calcites can be a proxy for permafrost conditions, as they require an ice body inside the cave to form[43]. The occurrence of cryogenic cave calcites in Central Europe[42,44,45] indicates that the climate conditions during MIS 3 stadials were, at least temporarily, cold enough to form permafrost and inhibit flowstone formation (Fig. 3).

However, other processes, such as re-routing of drip water within the aquifer, can also inhibit speleothem formation. Thus, the absence of growth does not necessarily indicate cold and/or dry conditions. In contrast, speleothem growth always requires favourable climate conditions and the periods of speleothem growth in Bleßberg Cave generally align with warm GIs. During these phases, any permafrost above the cave, which might have been present during stadial conditions, must have been absent. After climatic amelioration, the growth of the Bleßberg flowstones will most likely be delayed due to permafrost and/or the absence of vegetation cover above the cave. At the onset of a GI, even if the warming will reach Central Europe relatively quickly, the initiation of speleothem growth will thus be delayed due to the buffered warming by the karst above the cave as well as the time required for permafrost thawing and vegetation development. Therefore, the growth phases of the Bleßberg flowstones can be considered a sensitive proxy for the minimum duration of warm climate conditions in Central Europe during MIS 3.

Based on their age models (Figs. S6 – S8), most of the Bleßberg flowstone growth phases can be unambiguously assigned to GIs (Fig. 3 and Table S2). This clearly shows that flowstone growth in Bleßberg Cave primarily occurred during warm phases, while it was inhibited during stadial periods. This is reasonable considering the requirements for speleothem growth mentioned above. We can assign most growth phases to specific GIs based on the most abundant Monte-Carlo ages (i.e., the center bins of the age distribution, Fig. 3). In case of less precise age models (e.g., growth phases 4 and 8 of BB-9), the identification of the corresponding GIs is constrained by the surrounding growth phases (Fig. 3). The Bleßberg flowstones show growth during GIs 17 – 5, the only exception being GI 9. The lack of speleothem growth during GI 9 may be related to its short duration (260 years[3]) and the limited temperature increase in Greenland of 6.5 °C[4], which might not be sufficient to cross the threshold for conditions favourable for speleothem growth in Central Europe.

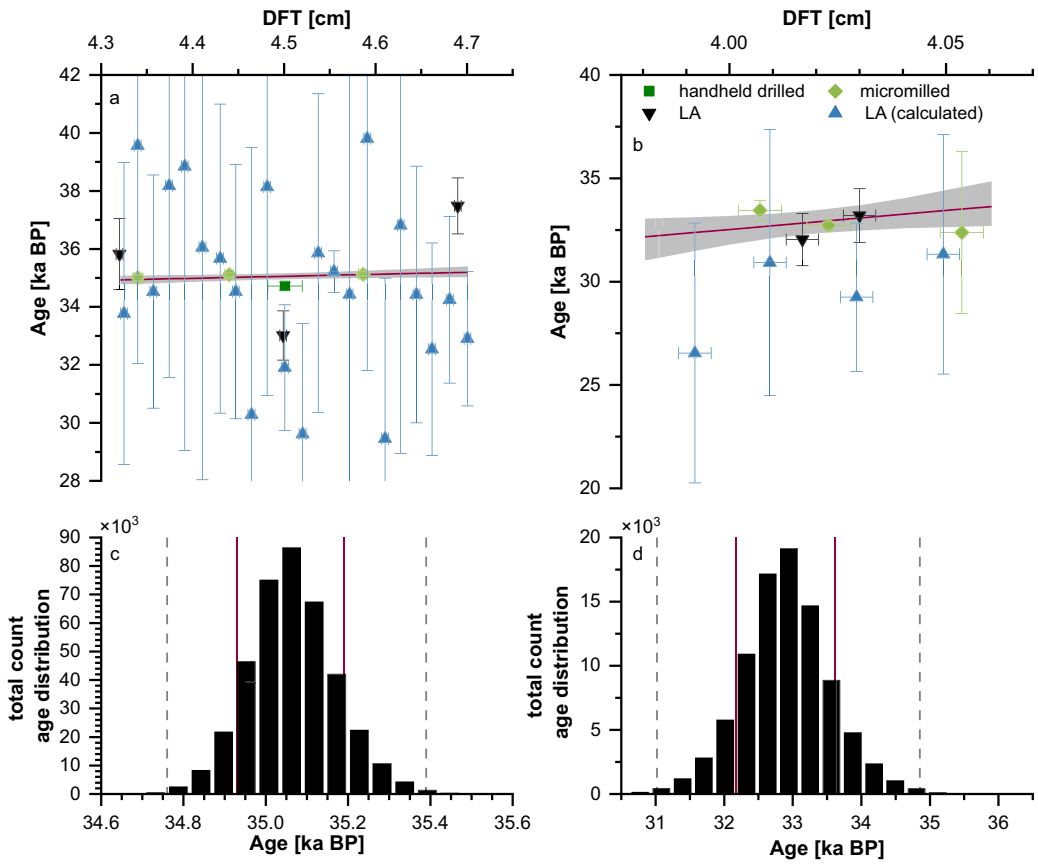

Fig. 2 | Age models and age distributions for two growth phases of sample BB-9. **a** and **b:** Age models (red line) for growth phases 6 (**a**) and 8 (**b**) of sample BB-9 and the corresponding 95% confidence intervals (grey area). Both are also indicated by the red and dashed lines in **c** and **d**. All ages used for the calculations including their uncertainty in depth (Table S3) are also shown: handheld drilled (dark green squares), micromilled (light green diamonds), LA ^{230}Th/U-ages parallel (black upside-down triangles) and LA ^{230}Th/U-ages perpendicular (blue triangles) to the growth layers. **c** and **d:** Histograms showing the individual ages calculated for growth phases 6 (**c**) and 8 (**d**) during the Monte-Carlo simulation. The number of bins for each histogram was set to 20.

Previous studies showed that speleothems can be used to precisely determine the onset of individual GI (sub-)events[18]. However, this is only possible if growth is continuous over the transition from stadial to interstadial conditions (i.e., the onset of the event). This may be the case for monsoon systems[46] or underneath temperate glaciers[33]. Based on these data, the onset of the GIs appears to be synchronous within a century between the European Mediterranean region, and the Asian and South American Monsoon regions[18]. However, in Central Europe, speleothem growth during MIS 3 is strongly related to the climatic conditions above the cave and thus restricted to warm phases, as has been shown for Bunker Cave[36]. Similar growth restrictions are true for Bleßberg Cave. During phases of comparably warm and wet climate, such as the Holocene, continuous speleothem growth in Bleßberg Cave is possible[47]. In contrast, the short duration of favourable conditions during MIS 3 in combination with small growth rates (~ 10 µm/a) of the flowstone samples causes very thin growth layers. Given the proximity to Greenland and the North Atlantic, it is reasonable to assume that the climate signal reaches Central Europe relatively quickly. However, there is still a debate about whether there is a delay (~ 200 years) before these changes are recorded[48,49] or whether they coincide within uncertainty, as suggested for both Central Europe[50] and the Asian and South American monsoon regions[18].

Central European warm phases

We created a combined density plot using the age distribution counts of all three flowstone samples (Fig. 4d–f) and the *Frequency Counts* function provided by the software Origin. This reduces the impact of less well-constrained growth phases. For instance, growth phase 4 of BB-9 (Fig S9), which is probably associated with GI 10, is not visible in the combined record due to the large age scatter spanning multiple GIs (Fig. 4d). Growth during GI 15, associated with growth phase 1.2 of BB-15 (Fig. 4f), is still visible in the combined record, but the corresponding peak is small and shifted towards the stadial period. The composite record represents phases of exceptionally warm and humid climate in Central Europe based on the Bleßberg speleothem growth phases (Fig. 4i). In total, eight growth phases can be identified distinctively correlating with GIs 16, 14 – 11 and 8 – 6. In the following we refer to these phases as Central European warm phases.

These Central European warm phases correlate with periods of a strong AMOC and diminished influence of AABW (Fig. 4a)[15], higher sea level (Fig. 4b)[51], warm sea surface temperatures (SST, Fig. 4c)[52], reduced sea ice cover (Fig. 4d)[53] and the absence of ice-rafted debris (IRD, Fig. 4h)[54]. Vegetation records from the Eifel Maar lakes (Fig.4e – g and S1)[55], which are located approximately 300 km west of Bleßberg Cave (see Supplementary material for details), indicate a warm temperate mixed forest during early MIS 3 (around 60 – 48 ka BP) in Central Europe, which was characterised by an increased abundance of *Picea* and *Carpinus* and a low abundance of *Poacaea*. This phase is also characterised by a very low abundance of IRD and correlates with the longer growth phases of the Bleßberg speleothems during GIs 16, 14 and 13 (Fig. 4i). Speleothem growth was absent during Heinrich event 5 (H5), and the increased abundance of *Poacaea* suggest generally cold climate. This is supported by reduced SST, a peak in the IRD record and increased sea ice cover (Fig. 4). The middle part of MIS 3 (ca. 47 – 40 ka BP) was characterised by a continuous abundance of *Picea* and sporadic abundance of *Carpinus*. During GI 12, the abundance of *Poacaea* briefly decreased, but then increased again indicating a cold temperate

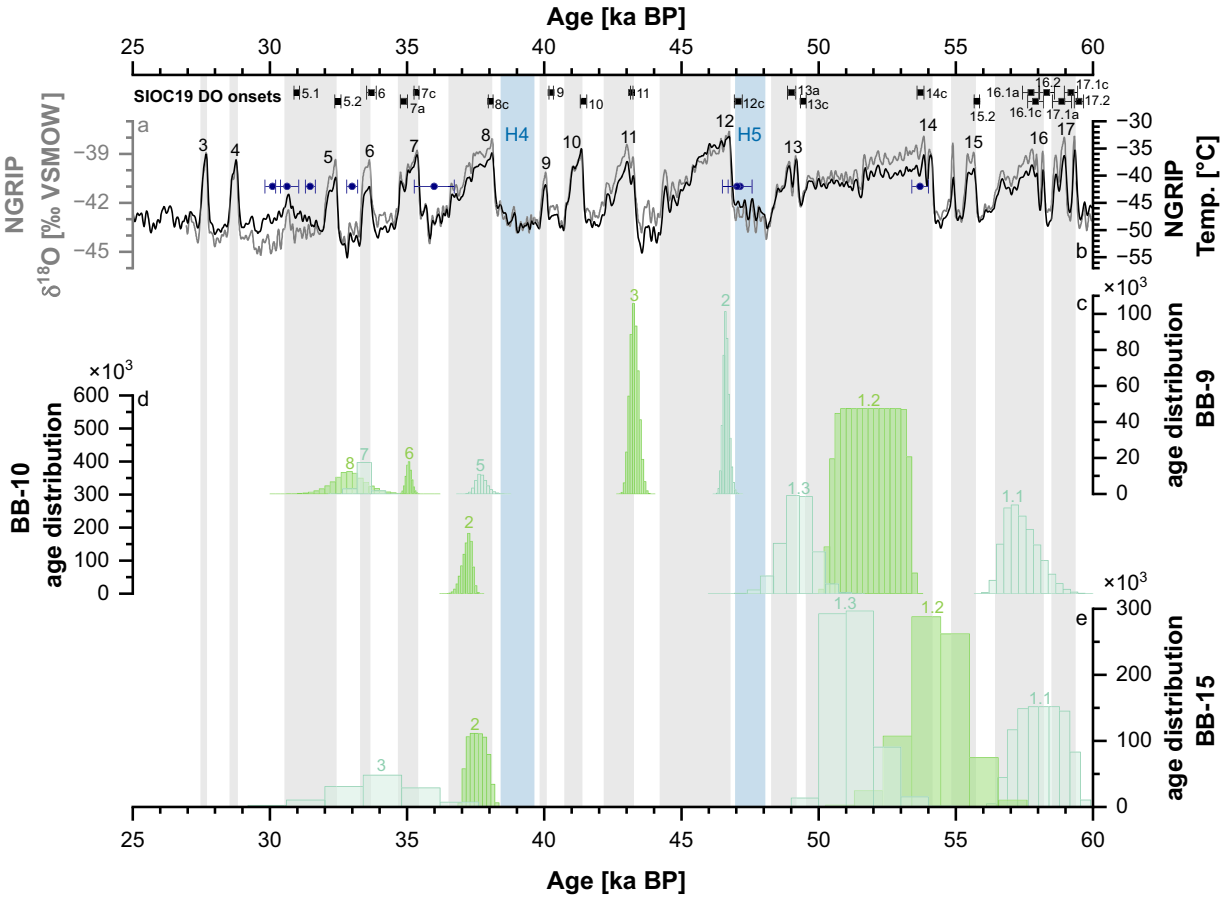

Fig. 3 | Distribution of ages for all three Bleßberg flowstone samples plotted in comparison with GI and Heinrich events. The timing of the GIs (grey bars) is based on the NGRIP GICC05 $\delta^{18}O$ values (**a**, grey line)[3] and temperature reconstruction (**b**, black line)[4]. Because there is no exact agreement regarding the timing and duration of Heinrich events[4,81,82], the blue bars for these events are based on the stadial in which they took place based on the NGRIP GICC05 chronology. The black dots represent speleothem GI onsets based on the SIOC19 record[18], and the blue dots show $^{230}Th/U$-ages of cryogenic cave calcites[42].

forest. Speleothem growth during this phase was restricted to two short growth phases corresponding to GIs 12 and 11. Speleothem growth was absent during H4, which was preceded by the relatively short GI 9 and is characterised by a large peak in IRD. The vegetation was sparse and dominated by *Poacaea*. During late MIS 3 (38 – 32 ka BP), the vegetation in the Eifel region consisted of *Poacaea*-dominated grassland. Nevertheless, we observe three speleothem growth phases, which occurred during times of reduced abundance of *Poacaea*. In general, the most prominent speleothem growth phases occurred during phases of low IRD, reduced sea ice and higher SST (Fig. 4).

The most prominent growth phase of the Bleßberg composite record (Fig. 4i) is from ca. 53.5 – 50.5 ka BP and corresponds with GI 14, which is the longest (4.6 ka) GI during MIS 3. GI 14 was characterised by persistently high summer SSTs (Fig. 4d), a reduced sea ice cover (Fig. 4c) and a persistently, relatively high (~ 50%) abundance of *Picea* (Fig. 4f). The abundance of *Carpinus* reaches the highest level (~ 30%) of MIS 3 during GI 14, suggesting the warmest climate conditions of MIS 3. The onset of GI 14 is characterised by a sharp decrease in AABW contribution into the Atlantic and a delayed, but substantial (ca. 10 m) rise in sea level. The prominent Bleßberg growth phase (Fig. 4i) correlates very well with these observations, documenting that long, continuous speleothem growth phases in Bleßberg Cave were only possible during the warmest and most stable phase of MIS 3. This is supported by the observation that speleothem growth stopped coincidently with the high abundance of *Carpinus*, even if the abundance of *Picea*, which needs less warm conditions, remained on the same level. While a recent study[56] suggested that DO 14 is only weakly expressed in European speleothem records, we clearly show that the long growth phase of the Bleßberg speleothems during GI 14 was related to long-lasting favourable climatic conditions for speleothem growth. This is further supported by the Bunker Cave record, which shows exceptionally fast speleothem growth during GI 14 (up to 390 µm/a) suggesting that this was the warmest and most humid phase of MIS 3 in Central Europe[36].

The growth phase during GI 12 is relatively short (0.74 ka), even if GI 12 was the second longest event (2.6 ka) of MIS 3 and associated with the highest summer SST (Fig. 4). The timing of our growth phase is consistent with the warmest phase of the event, as suggested by a minimum in sea ice cover and the peak abundance of *Picea* (ca. 60%). Interestingly, the stop of speleothem growth coincides with a large IRD peak (Fig. 4). This may indicate a climatic reason for the cessation of speleothem growth. Due to dating uncertainties in the sediment record[54], it cannot be excluded that the IRD peak corresponds to H5 and thus occurred before our growth phase. A peak in the abundance of *Carpinus* towards the end of GI 12 (ca. 45 ka BP) suggests a short phase of warm climate, but speleothem growth did not resume. This short climate amelioration was either too short for speleothem growth to resume, but it may also indicate that speleothem growth in this case may be affected by other processes than climate, such as re-routing of the drip water within the aquifer and thus, the absence of growth does not necessarily indicate

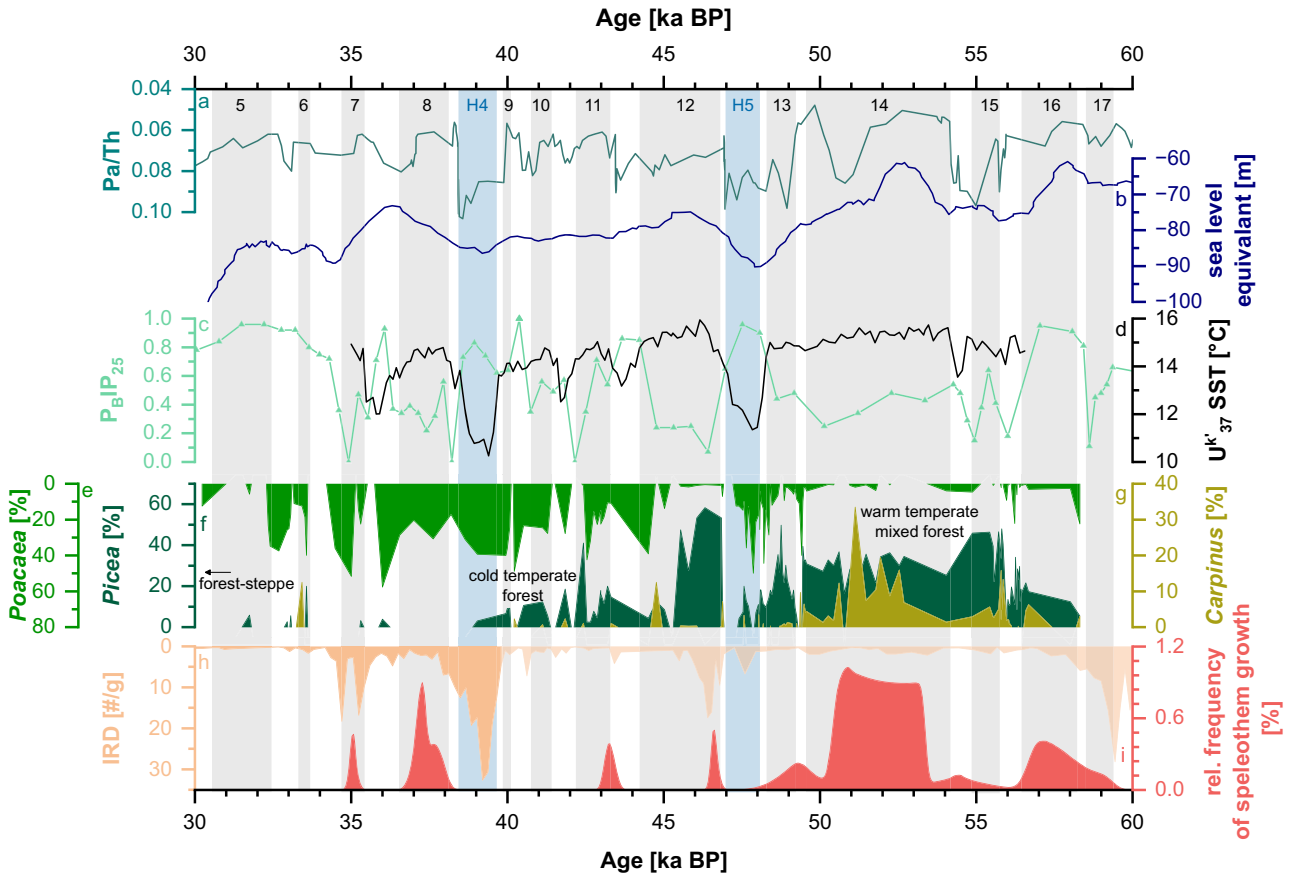

Fig. 4 | Bleßberg speleothem growth phases in comparison to other climate records. a AABW reconstruction based on a Pa/Th record from core CDH19 from the Bermuda Rise (dark turquoise line)[15]. **b** Red Sea sea level reconstruction (dark blue line)[51]. **c** North Atlantic sea ice cover reconstruction based on P_bIP_{25} (brassicasterol C25 isoprenoid lipid) from the SE Norwegian Sea (light turquoise line with triangles)[53]. **d** Summer alkenone-based SST ($U^{k'}_{37}$) from core MD01-2444 at the Iberian Margin (37°N, black line)[52]. **e, f** and **g** Vegetation reconstructions based on pollen data from *Poacaea* (green), *Picea* (dark green) and *Carpinus* (yellow-green) from different Eifel Maar cores (AU3, AU4, HM4)[55]. **h** Ice rafted debris (IRD) record from core MD01-2040 at the Iberian Margin (40°N, light orange)[54] **i** Combined relative frequency of growth of all three Bleßberg flowstone samples (red, Table S4). GI (grey) and Heinrich (blue) events are indicated by the coloured bars.

less favourable climate conditions for speleothem growth. The occurrence of speleothem growth, however, certainly shows that the climatic conditions were favourable at some point (i.e., no permafrost and at least some vegetation cover above the cave).

The only growth phase of the composite record, which is recorded in all three speleothem samples, is the growth phase concordant with GI 8. The timing of the onset in sample BB-10 is ca. 0.5 ka later than in BB-9 and BB-15 (Table S2). As the climatic conditions above the cave are identical for all three samples, this could be caused by a difference in the routing of the drip water. GI 8 followed H4, and vegetation in Central Europe was dominated by grassland and trees suggesting colder conditions[55]. H4 is reflected by a substantial amount of IRD in the Atlantic (Fig. 4h), which gradually reduced with the beginning of our speleothem growth phase associated with GI 8. The timing of the growth phase agrees with the peak of summer SST and the reduction of AABW. Since previous studies[36,56,57] showed no speleothem growth prior to H4 in Central Europe, this is also the first evidence of MIS 3 speleothem growth in Central Europe.

During GI 7, a short growth phase at Bleßberg Cave was recorded, which fits very well with a short reduction of IRD in the middle of the GI. Similarly, the timing of the growth phase is in agreement with a brief reduction in the abundance of *Poacaea* and the minimum of sea ice cover during the GI. GI 7 is one of the shortest events (740 years duration) when speleothem growth in Bleßberg Cave was recorded. In addition, the vegetation reconstruction from the Eifel maar lakes does not indicate particularly warm conditions. While the duration of 260 years of GI 9 seems to be too short to establish favourable speleothem growth conditions, the short, but still longer GI 7 is recorded in the Bleßberg record. This suggests that even short speleothem growth phases can occur without a well-established vegetation cover when short phases of favourable climate conditions occur and highlight their potential as a climate proxy.

The majority of the Bleßberg speleothem growth phases and thus show a lag (see methods for details) compared to the GI onsets recorded in Greenland ice cores (Fig. 4, Table S4). The magnitude of the lag is not related to the magnitude or length of the cold periods prior to the event (e.g., for Heinrich events). Similarly, we do not observe a relationship with the magnitude of the temperature increase of the corresponding GI. A recent study[58] shows that GICC05 is on average systematically younger than the U-Th timescale, at least for the last 48 ka. Therefore, the lag observed in this study should be treated as a maximum difference between the GI onset and the occurrence of favourable growth conditions for speleothems in Central Europe. The absence of the shortest and coldest GIs in the Bleßberg speleothem record suggests that the delay of the Bleßberg growth phases is rather related to the time required to establish favourable conditions for speleothem growth (i.e., inherent to the speleothem archive) than the time required to transfer the climate signal from the North Atlantic to Central Europe. This includes the availability of liquid water, the thawing of

permafrost, and the development of soil and vegetation cover above the cave. The total duration of the Bleßberg speleothem growth phases is generally shorter than the duration of the corresponding GIs. The duration of the speleothem growth phases covers approximately 88% of the total duration of GIs during early MIS 3 and is strongly reduced to 25% during mid and late MIS 3. This supports the assumption of a generally warmer early MIS 3 as suggested in previous studies[36,59]. This also indicates that during the onset of the GIs, the climate in Central Europe was still too cold, and potential permafrost conditions in combination with a strongly reduced or absent vegetation cover above the cave prohibited speleothem growth. The beginning of speleothem growth in Bleßberg Cave then marks the crossing of a certain climate threshold, and the following growth period reflects persistent warm climate conditions during the corresponding event in Central Europe. In most cases, speleothem growth ceased prior to the end of the corresponding GI, indicating that non-favourable conditions for speleothem formation returned towards the end of the event.

In summary, the flowstones from Bleßberg cave can provide a better understanding of the periods of warm and stable climate conditions during MIS 3 in Central Europe even if our data suggest a systematic lag between the onset of the speleothem growth phases and the GIs recorded in Greenland ice cores. Similarly, the duration of our growth phases is systematically shorter than that of the corresponding GIs suggesting that the speleothems mainly record the persistent warming of the events. The record of Bleßberg speleothem growth phases can thus be interpreted as snapshots of the Central European warm phases during MIS 3, and our results highlight that large portions of MIS 3 in Central Europe had favourable conditions to enable speleothem growth. Our data suggest that climatic conditions in Central Europe during MIS 3 were much longer favourable for speleothem growth than previously expected. So far, MIS 3 speleothem records from Central Europe suggested that speleothem growth occurred no later than 42.8 ka in Bunker Cave[36] and 37.1 ka in Han-sur-Lesse Cave[56], respectively, and that climatic conditions subsequently were too cold and dry for speleothem formation. The samples from Bleßberg Cave, however, show that speleothem deposition in Central Europe occurred at least until ca. 32 ka. This shows the great potential of speleothems from temperate climate zones, when speleothem growth can be used as a direct proxy to determine favourable climatic conditions. Especially during phases with oscillating climatic, as during the DO events within MIS 3, speleothem growth phases will record the peaks of favourable climate conditions. However, the oscillating climate conditions will cause speleothem growth to frequently start and stop within a relatively short amount of time. This will result in very thin growth layers interrupted by hiatuses and complex growth characteristics on the µm-scale. To make use of the full potential of this remarkable climate archive, a variety of sampling and analytical techniques is required.

Methods

Sampling procedure

All sampling procedures and measurements described in the following were conducted at the Institute for Geosciences, Johannes Gutenberg University Mainz.

Due to the typically very thin growth layers of our flowstone samples, we applied different sampling techniques. Since BB-10 and BB-15 show longer/thicker sections of continuous growth, the majority of samples was taken using a handheld drill (sample sizes of approximately 50 mg). For BB-9, the thickness of the individual MIS 3 growth phases is much thinner and varies between 3.9 and 0.6 mm. Therefore, we used a MicroMill device[60] with a drill bit of 300 or 500 µm thickness for sampling (approximately 15 mg). However, even with these sampling techniques, it was not always possible to completely avoid detrital contamination, indicated by $(^{230}Th/^{232}Th) < 200$ (compare Table S1a, c and e).

Solution ^{230}Th/U-dating

Powdered samples were processed in a clean room laboratory for chemical separation of U and Th (see Table S5 for details). All acids used during chemical treatment were of trace-metal grade quality. Samples were weighed, dissolved in 7 N HNO_3 and subsequently spiked with a previously calibrated ^{229}Th-^{233}U-^{236}U spike solution. The spike was gravimetrically prepared and then calibrated against IRMM074/10[61] and a solution prepared from speleothem sample WM 1 from Wilder Mann Cave, which has an approximate age of 2.02 Ma[62] and is therefore in secular equilibrium[63] i.e., $(^{234}U/^{238}U) = (^{230}Th/^{238}U) = 1$. The samples were evaporated to dryness and treated with concentrated HNO_3, HCl and H_2O_2 in order to destroy any organic material prior to chemical separation. The samples were then evaporated again, dissolved in 7 N HNO_3 and passed through ion exchange columns filled with 1.5 mL of Bio-Rad AG 1-X8 (200 – 400 mesh size) anion exchange resin to separate U and Th. The procedure (Table S5) was carried out twice and followed a method developed at the Berkely Geochronology Center, which is based on the procedure described in Edwards et al.[64]. With each sample set, a subsample of the WM 1 solution was prepared and analysed for quality control, yielding activity ratios of $(^{230}Th/^{238}U) = 1.00001 \pm 0.00038$ and $(^{234}U/^{238}U) = 0.99997 \pm 0.00021$ (2SE, $n = 55$, within a 12-month period).

Mass spectrometric analyses of U and Th were conducted using a Thermo Fischer Scientific Neptune Plus multi-collector inductively coupled plasma mass spectrometer (MC-ICP-MS) equipped with an Elemental Scientific Apex Omega HF desolvator. U and Th were measured separately in a standard-bracketing procedure and the data were corrected offline using an in-house R-script[65] correcting for mass fractionation, ion counter yield, instrumental drift and tailing. Each sample is analysed in standard-sample-bracketing (SBB) mode, accounting for instrumental drift during the analytical session. For U, the CRM112-A Uranium Isotopic Standard is analysed prior to and after each sample, while for Th an in-house Th standard solution with known isotope ratios of ^{229}Th, ^{230}Th and ^{232}Th is analysed. Mass fractionation is determined for each standard by analysing $^{235}U/^{238}U$ or $^{229}Th/^{232}Th$, respectively. Within the same analysis, ion counter yield for IC1 is determined by analysing $^{234}U/^{238}U$ or $^{230}Th/^{232}Th$, both previously corrected for mass fractionation. Tailing is determined externally by analysing a concentrated CRM 112-A U solution (containing ^{234}U, ^{235}U, ^{238}U) or a natural Th solution (containing ^{232}Th) at the beginning and at the end of each analytical session. Abundance sensitivity is calculated and corrected for isotopes of ^{229}Th, ^{230}Th, ^{233}U and ^{236}U.

All ages were calculated using the half-lives reported by Cheng et al.[63]. Due to the very thin growth layers of our flowstone samples (especially BB-9), some samples show $(^{230}Th/^{232}Th) < 10$ (Table S1a) and are thus significantly affected by detrital contamination. This is particularly the case for samples close to hiatuses. To better constrain the $(^{232}Th/^{238}U)$ activity ratio of the detrital material, we applied the approach of Budsky et al.[66] to the solution data of all three samples. This algorithm minimises the sum of all apparent age inversions by iteratively varying the $(^{232}Th/^{238}U)$ activity ratio of the detrital material, $(^{232}Th/^{238}U)_d$[67]. The resulting $(^{232}Th/^{238}U)_d$ is 0.953 ± 0.477, which is applied to all three samples and in agreement within uncertainty with the conventionally used correction factor of $(^{232}Th/^{238}U)_d = 1.243 \pm 0.622$ calculated based on the average Th and U concentrations for the bulk upper continental crust[68–70].

Laser Ablation MC-ICP-MS ^{230}Th/U-dating

In-situ analyses for ^{230}Th/U-dating have been performed using the Neptune Plus MC-ICP-MS coupled to an ESI New Wave NWR 193 nm ArF excimer laser ablation system (LA-MC-ICP-MS) with a TwoVol2 cell. To enhance sensitivity and introduce N_2 for signal stabilisation, an ESI Apex Omega HF desolvator system was additionally coupled with the sample outlet being connected with a Y-connector to the sample gas line originating from the laser ablation system. Instrumental details are summarised in Table S6.

Due to the low abundance of the decay products ^{234}U and ^{230}Th, both isotopes are monitored using the central ion counter. Therefore, two separate line scans are necessary to calculate ^{230}Th ages with the instrumental setup during this study (cup configuration in Table S7). Prior to each analysis, 30 s of background data was collected without the laser firing and

subtracted from the signals monitored during sample ablation. Speleothem sample WM 1 was used as bracketing standard, as this speleothem is in secular equilibrium. A first line scan (line scan 1, Table S8) performed on WM 1 was used to determine the mass fractionation factor β based on the naturally invariant $^{235}U/^{238}U$, and a correction factor for ($^{230}Th/^{238}U$) correcting for mass fractionation, ion counter yield and inter-element fractionation, which was then applied to the unknown speleothem samples. Similarly, a second line scan (line scan 2, Table S8) on WM 1 was used to determine a correction factor for ($^{234}U/^{238}U$), correcting for mass fractionation and ion counter yield. Similar to the solution $^{230}Th/U$-dating, the ($^{232}Th/^{238}U$) from the speleothem samples was used to correct for detrital contamination, using the previously determined detrital correction factor of $(^{232}Th/^{238}U)_d = 0.953 \pm 0.477$.

LA-MC-ICP-MS allows fast data acquisition and less destructive sampling compared to the drilling techniques. For each age determination, two line scans parallel to the growth layers were conducted (1000 µm length, 150 µm spot size, 100 Hz laser frequency) in close proximity to determine ($^{230}Th/^{238}U$) and ($^{234}U/^{238}U$) in two separate measurements. LA-MC-ICP-MS ^{230}Th-dating was applied to samples BB-9 and −10. A global correction factor for $^{230}Th/^{238}U$ and $^{234}U/^{238}U$ was determined for each standard of WM 1. The obtained isotope ratios of $^{230}Th/^{238}U$ and $^{234}U/^{238}U$ were calculated into activity ratios using the decay constants from Cheng et al.[63], resulting in a global correction factor accounting for mass bias, ion counter yield and inter-element fractionation. This correction factor was then applied to sample activity ratios of ($^{230}Th/^{238}U$) and ($^{234}U/^{238}U$).

In addition to the line scan measurements along the growth layers, several line scans were conducted parallel to the growth axis (i.e., vertical to the growth layers) across the hiatuses (Fig. S3c). The data from these transects was used to calculate mean $^{230}Th/U$-ages at 0.2 mm spatial resolution between a selected depth, which increased the number of individual ages. Large and rapid changes (Fig. S4) in the calculated initial ($^{234}U/^{238}U$) activity ratios, $(^{234}U/^{238}U)_i$, calculated as $(^{234}U/^{238}U)_i = (^{234}U/^{238}U) * \exp(\lambda_{234} * t)$, where t is the $^{230}Th/U$-age, were used to determine growth stops, which are not visible or reflected by changes in the trace element data.

Trace element analysis and mapping

Trace element analysis was conducted by LA-ICP-MS using an ESI New Wave NWR 193 nm ArF Excimer laser system coupled to an Agilent 7500ce ICP-MS. A continuous line scan from top to bottom was conducted for samples BB-9 and BB-10 with the intensities of ^{27}Al, ^{232}Th and ^{238}U monitored. The laser parameters used were a rectangular spot size of 130 × 50 µm, a transition rate of 10 µm/s and a laser repetition rate of 10 Hz, resulting in a fluence of 3.5 J/cm^2. For calibration purposes, NIST SRM 610 was analysed several times during the analyses, together with several other quality control materials, including NIST SRM 612, BCR-2G and MACS3. For all analyses, ^{43}Ca was used as an internal reference, and data evaluation was performed offline following the calculations presented in Mischel et al.[71]. Prior to each analysis, a pre-ablation was performed. A principal component analysis (PCA) of the trace element data was conducted using the prcomp() function of the statistical software R[72] in order to identify the detrital component within the trace elements.

The mapping of the trace element distribution (^{27}Al, ^{238}U) was performed using the Matlab script MapIT![73] using the same instrumental LA-ICP-MS setup as described above. NIST SRM 610 was used for calibration purposes. The final map consists of a total number of 33 line scans with a circular spot size of 80 µm resulting in a mapping area of 25,000 × 2640 µm. A transition rate of 50 µm/s was used. No pre-ablation was performed prior to the mapping.

Age-depth modelling

The individual growth phases of our flowstone samples are exceptionally thin. For the majority of growth phases, it is, thus, not possible to determine several high-precision solution $^{230}Th/U$-ages, even if sampling is conducted using the MicroMill. In addition, the solution ages are often affected by detrital contamination resulting in substantially increased uncertainties. This is particularly problematic for the thinnest growth phases. However, for all growth phases several high-resolution LA-MC-ICP-MS $^{230}Th/U$-ages are available, even if those are associated with much larger uncertainties than the solution ages (Fig. 2a and b). The age data for the individual flowstone growth phases, thus, usually consist of a few (sometimes only a single) high-precision solution ages and several less precise LA-MC-ICP-MS ages. The uncertainty of the LA-MC-ICP-MS ages is, on average, larger by a factor of >10 compared to the solution ages. This also implies that each growth phase shows various age inversions within uncertainty (Fig. 2a and b).

The conventionally used methods for age-depth modelling in speleothems are designed for ages with a spatial resolution of a few mm to a few cm, comparable age uncertainty and only a limited number of age inversions (for details see in refs. 74,75). Thus, these algorithms, such as linear interpolation, StalAge[76] or COPRA[77], cannot be applied to the very high-spatial resolution age data of our flowstone samples.

Here we use a modified version of an error-weighted linear regression (i.e., the York[78] fit), which accounts for uncertainties in both x- and y-direction (i.e., the *york()* function implemented in R-package *IsoplotR*[79]). Since the growth rate of the speleothem cannot be negative (i.e., it needs to become progressively older with increasing distance from top), negative slopes of the fit must be excluded. To account for this, we perform a Monte-Carlo simulation with the results of the York-fit (i.e., slope, intercept and the corresponding covariance) and exclude those simulations with a negative slope. Based on these simulations, we also calculate the Mean Square of Weighted Deviates (MSWD) and the probability of fit for the fits with a positive slope (Table S9). These two parameters allow to assess whether the assumptions of a linear regression are justified by the assigned analytical errors, i.e., if the observed scatter around the regression is comparable with the age uncertainties (for a detailed discussion see Ludwig[80]). In case of probabilities of fit <0.05, indicating excess scatter, we use the established methods for excess scatter isochrons and expand the uncertainties by the square root of the MSWD and the corresponding Student's t factor for a confidence level of 95%[80]. In other words, if the ages and uncertainties suggest that the age data of a growth phase cannot be described by a linear regression (e.g., due to a change in the growth rate), the uncertainties of the age model are increased accordingly.

We then use the results of our Monte-Carlo simulations to calculate the median age model, the corresponding 95%-confidence limits and the probability distributions/histograms of the simulated age data (Figs. 2 and 3).

Determination of durations and lags compared to GIs

The Central European warm phases were established based on the *Frequency Counts* function provided by the software Origin. This function calculates the frequency of data within a specified range, i.e., the age ranges of the individual growth phases based on the Monte-Carlo simulations. It computes a set of bins using the minimum and maximum values and a specified bin size, which was set to 100 years. Then, it examines each bin to count how many times a value falls within each bin. For the calculation only growth phases with >30% positive slopes were used (Table S9, Fig. S12). The timing of the baselines and peaks of each warm phases were determined using the Origin *Peak Analyzer* function. The onset and end of the warm phase are determined at half peak height and subsequently used for the calculation of the duration of each warm phases (Fig. S13). The comparison of the onset and duration of the warm phases and the GIs were based on these calculations (Table S4).

Data availability

The $^{230}Th/U$ data compiled for this study are provided in Supplementary Table S1a – f. The calculated age models, histogram data files and analysed LA U/Th line scan data are available in an online open-access repository at https://doi.org/10.6084/m9.figshare.27223863.v1.

Received: 26 January 2024; Accepted: 31 October 2024;
Published online: 20 November 2024

References

1. Dansgaard, W. et al. Evidence for general instability of past climate from a 250-kyr ice-core record. *Nature* **364**, 218–220 (1993).
2. NGRIP Project members. High-resolution record of Northern Hemisphere climate extending into the last interglacial period. *Nature* **431**, 147–151 (2004).
3. Rasmussen, S. O. et al. A stratigraphic framework for abrupt climatic changes during the Last Glacial period based on three synchronized Greenland ice-core records: refining and extending the INTIMATE event stratigraphy. *Quat. Sci. Rev.* **106**, 14–28 (2014).
4. Kindler, P. et al. Temperature reconstruction from 10 to 120 kyr b2k from the NGRIP ice core. *Clim* **10**, 887–902 (2014).
5. Andersen, K. K. et al. The Greenland Ice Core Chronology 2005, 15–42ka. Part 1: constructing the time scale. *Quat. Sci. Rev.* **25**, 3246–3257 (2006).
6. Erhardt, T. et al. Decadal-scale progression of the onset of Dansgaard–Oeschger warming events. *Clim* **15**, 811–825 (2019).
7. Johnsen, S. et al. Irregular glacial interstadials recorded in a new Greenland ice core. *Nature* **359**, 311–313 (1992).
8. Birchfield, G. E. & Broecker, W. S. A salt oscillator in the glacial Atlantic? 2. A "scale analysis" model. *Paleoceanography* **5**, 835–843 (1990).
9. Broecker, W. S., Peteet, D. M. & Rind, D. Does the ocean–atmosphere system have more than one stable mode of operation? *Nature* **315**, 21–26 (1985).
10. Menviel, L., Timmermann, A., Friedrich, T. & England, M. Hindcasting the continuum of Dansgaard–Oeschger variability: mechanisms, patterns and timing. *Climate* **10**, 63–77 (2014).
11. Zhang, X., Knorr, G., Lohmann, G. & Barker, S. Abrupt North Atlantic circulation changes in response to gradual CO2 forcing in a glacial climate state. *Nat. Geosci.* **10**, 518–523 (2017).
12. Zhang, X., Lohmann, G., Knorr, G. & Purcell, C. Abrupt glacial climate shifts controlled by ice sheet changes. *Nature* **512**, 290–294 (2014).
13. Boers, N., Ghil, M. & Rousseau, D.-D. Ocean circulation, ice shelf, and sea ice interactions explain Dansgaard–Oeschger cycles. *Proc. Natl Acad. Sci.* **115**, E11005–E11014 (2018).
14. Sime, L. C., Hopcroft, P. O. & Rhodes, R. H. Impact of abrupt sea ice loss on Greenland water isotopes during the last glacial period. *Proc. Natl Acad. Sci.* **116**, 4099–4104 (2019).
15. Henry, L. et al. North Atlantic ocean circulation and abrupt climate change during the last glaciation. *Science* **353**, 470–474 (2016).
16. Vettoretti, G., Ditlevsen, P., Jochum, M. & Rasmussen, S. O. Atmospheric CO_2 control of spontaneous millennial-scale ice age climate oscillations. *Nat. Geosci.* **15**, 300–306 (2022).
17. Fohlmeister, J. et al. Global reorganization of atmospheric circulation during Dansgaard–Oeschger cycles. *Proc. Natl Acad. Sci.* **120**, e2302283120 (2023).
18. Corrick, E. C. et al. Synchronous timing of abrupt climate changes during the last glacial period. *Science* **369**, 963–969 (2020).
19. Kathayat, G. et al. Indian monsoon variability on millennial-orbital timescales. *Sci. Rep.* **6**, 24374 (2016).
20. Bond, G. et al. Correlations between climate records from North Atlantic sediments and Greenland ice. *Nature* **365**, 143–147 (1993).
21. Spötl, C. & Mangini, A. Stalagmite from the Austrian Alps reveals Dansgaard–Oeschger events during isotope stage 3:: Implications for the absolute chronology of Greenland ice cores. *Earth Planet. Sci. Lett.* **203**, 507–518 (2002).
22. Adolphi, F. et al. Connecting the Greenland ice-core and U/Th timescales via cosmogenic radionuclides: testing the synchroneity of Dansgaard–Oeschger events. *Climate* **14**, 1755–1781 (2018).
23. Sachs, J. P. & Lehman, S. J. Subtropical North Atlantic temperatures 60,000 to 30,000 years ago. *Science* **286**, 756–759 (1999).
24. Barker, S. et al. Icebergs not the trigger for North Atlantic cold events. *Nature* **520**, 333–336 (2015).
25. Peterson, L. C., Haug, G. H., Hughen, K. A. & Rohl, U. Rapid changes in the hydrologic cycle of the tropical Atlantic during the last glacial. *Science* **290**, 1947–1951 (2000).
26. Barker, S. et al. Interhemispheric Atlantic seesaw response during the last deglaciation. *Nature* **457**, 1097–1102 (2009).
27. Kanner, L. C., Burns, S. J., Cheng, H. & Edwards, R. L. High-latitude forcing of the South American summer monsoon during the last glacial. *Science* **335**, 570–573 (2012).
28. Wang, X. et al. Interhemispheric anti-phasing of rainfall during the last glacial period. *Quat. Sci. Rev.* **25**, 3391–3403 (2006).
29. Moseley, G. E. et al. NALPS19: Sub-orbital-scale climate variability recorded in northern Alpine speleothems during the last glacial period. *Climate* **16**, 29–50 (2020).
30. Svensson, A. et al. A 60 000 year Greenland stratigraphic ice core chronology. *Climate* **4**, 47–57 (2008).
31. Richards, D. A. & Dorale, J. A. Uranium-series chronology and environmental applications of speleothems. *Rev. Mineral. Geochem.* **52**, 407–460 (2003).
32. Scholz, D. & Hoffmann, D. ^{230}Th/U-dating of fossil corals and speleothems. *EG Quat. Sci. J.* **57**, 52–76 (2008).
33. Moseley, G. E. et al. Multi-speleothem record reveals tightly coupled climate between central Europe and Greenland during Marine Isotope Stage 3. *Geology* **42**, 1043–1046 (2014).
34. Genty, D. et al. Precise dating of Dansgaard–Oeschger climate oscillations in western Europe from stalagmite data. *Nature* **421**, 833–837 (2003).
35. Budsky, A. et al. Western Mediterranean climate response to Dansgaard/Oeschger events: New insights from speleothem records. *Geophys. Res. Lett.* **46**, 9042–9053 (2019).
36. Weber, M. et al. Evidence of warm and humid interstadials in central Europe during early MIS 3 revealed by a multi-proxy speleothem record. *Quat. Sci. Rev.* **200**, 276–286 (2018).
37. Sirocko, F. et al. Muted multidecadal climate variability in central Europe during cold stadial periods. *Nat. Geosci.* **14**, 651–658 (2021).
38. Prud'homme, C. et al. Millennial-timescale quantitative estimates of climate dynamics in central Europe from earthworm calcite granules in loess deposits. *Commun. Earth Environ.* **3**, 267 (2022).
39. Vandenberghe, J. et al. The L ast P ermafrost M aximum (LPM) map of the N orthern H emisphere: permafrost extent and mean annual air temperatures, 25–17 ka BP. *Boreas* **43**, 652–666 (2014).
40. Atkinson, T., Harmon, R., Smart, P. & Waltham, A. Palaeoclimatic and geomorphic implications of 230Th/234U dates on speleothems from Britain. *Nature* **272**, 24–28 (1978).
41. Vaks, A. et al. Speleothems reveal 500,000-year history of Siberian permafrost. *Science* **340**, 183–186 (2013).
42. Richter, D. K., Scholz, D., Jöns, N., Neuser, R. D. & Breitenbach, S. F. Coarse-grained cryogenic aragonite as end-member of mineral formation in dolomite caves. *Sediment. Geol.* **376**, 136–146 (2018).
43. Richter, D., Meissner, P., Immenhauser, A., Schulte, U. & Dorsten, I. Cryogenic and non-cryogenic pool calcites indicating permafrost and non-permafrost periods: a case study from the Herbstlabyrinth-Advent Cave system (Germany). *Cryosphere* **4**, 501–509 (2010).
44. Richter, D. K. et al. Weichselzeitliche Kryocalcite als Hinweise für Eisseen in der Hüttenbläserschachthöhle (Iserlohn/NRW). *EG Quat. Sci. J.* **64**, 67–81 (2015).
45. Žák, K. et al. Coarsely crystalline cryogenic cave carbonate–a new archive to estimate the Last Glacial minimum permafrost depth in Central Europe. *Climate* **8**, 1821–1837 (2012).
46. Cheng, H. et al. The Asian monsoon over the past 640,000 years and ice age terminations. *nature* **534**, 640–646 (2016).

47. Breitenbach, S. F. et al. Holocene interaction of maritime and continental climate in Central Europe: New speleothem evidence from Central Germany. *Glob. Planet. Change* **176**, 144–161 (2019).
48. Lane, C. S., Brauer, A., Blockley, S. P. & Dulski, P. Volcanic ash reveals time-transgressive abrupt climate change during the Younger Dryas. *Geology* **41**, 1251–1254 (2013).
49. Rach, O., Brauer, A., Wilkes, H. & Sachse, D. Delayed hydrological response to Greenland cooling at the onset of the Younger Dryas in western Europe. *Nat. Geosci.* **7**, 109–112 (2014).
50. Reinig, F. et al. Precise date for the Laacher See eruption synchronizes the Younger Dryas. *Nature* **595**, 66–69 (2021).
51. Grant, K. et al. Sea-level variability over five glacial cycles. *Nat. Commun.* **5**, 5076 (2014).
52. Martrat, B. et al. Four climate cycles of recurring deep and surface water destabilizations on the Iberian margin. *Science* **317**, 502–507 (2007).
53. Hoff, U., Rasmussen, T. L., Stein, R., Ezat, M. M. & Fahl, K. Sea ice and millennial-scale climate variability in the Nordic seas 90 kyr ago to present. *Nat. Commun.* **7**, 12247 (2016).
54. Schönfeld, J., Zahn, R. & de Abreu, L. Surface and deep water response to rapid climate changes at the Western Iberian Margin. *Glob. Planet. Change* **36**, 237–264 (2003).
55. Sirocko, F. et al. Thresholds for the presence of glacial megafauna in central Europe during the last 60,000 years. *Sci. Rep.* **12**, 20055 (2022).
56. Peral, M. et al. A new insight of the MIS 3 Dansgaard-Oeschger climate oscillations in western Europe from the study of a Belgium isotopically equilibrated speleothem. *Quat. Sci. Rev.* **329**, 108564 (2024).
57. Pons-Branchu, E., Hamelin, B., Losson, B., Jaillet, S. & Brulhet, J. Speleothem evidence of warm episodes in northeast France during Marine Oxygen Isotope Stage 3 and implications for permafrost distribution in northern Europe. *Quat. Res.* **74**, 246–251 (2010).
58. Muschitiello, F. & Aquino-Lopez, M. A. Continuous synchronization of the Greenland ice-core and U-Th timescales using probabilistic inversion. *Clim. Discuss.* **2023**, 1–32 (2023).
59. Sirocko, F. et al. The ELSA-Vegetation-Stack: Reconstruction of Landscape Evolution Zones (LEZ) from laminated Eifel maar sediments of the last 60,000 years. *Glob. Planet. Change* **142**, 108–135 (2016).
60. Dettman, D. L. & Lohmann, K. C. Microsampling carbonates for stable isotope and minor element analysis: Physical separation of samples on a 20 micrometer scale. *Journal of Sedimentary Research* **65** (1995).
61. Richter, S. et al. A new series of uranium isotope reference materials for investigating the linearity of secondary electron multipliers in isotope mass spectrometry. *Int. J. Mass Spectrom.* **281**, 115–125 (2009).
62. Meyer, M., Cliff, R., Spötl, C., Knipping, M. & Mangini, A. Speleothems from the earliest Quaternary: Snapshots of paleoclimate and landscape evolution at the northern rim of the Alps. *Quat. Sci. Rev.* **28**, 1374–1391 (2009).
63. Cheng, H. et al. Improvements in 230Th dating, 230Th and 234U half-life values, and U–Th isotopic measurements by multi-collector inductively coupled plasma mass spectrometry. *Earth Planet. Sci. Lett.* **371**, 82–91 (2013).
64. Edwards, R. L., Chen, J. & Wasserburg, G. 238U234U230Th232Th systematics and the precise measurement of time over the past 500,000 years. *Earth Planet. Sci. Lett.* **81**, 175–192 (1987).
65. Team, R. C. R. Development Core Team R: A Language and Environment for Statistical Computing 2023. *R Core Team: Vienna, Austria* (2023).
66. Budsky, A. et al. Speleothem $\delta^{13}C$ record suggests enhanced spring/summer drought in south-eastern Spain between 9.7 and 7.8 ka – A circum-Western Mediterranean anomaly? *Holocene* **29**, 1113–1133 (2019).
67. Klaes, B. et al. High-resolution stalagmite stratigraphy supports the Late Holocene tephrochronology of southernmost Patagonia. *Commun. Earth Environ.* **3**, 23 (2022).
68. Taylor, S. R. & McLennan, S. M. The continental crust: its composition and evolution. (1985).
69. Ludwig, K. & Paces, J. Uranium-series dating of pedogenic silica and carbonate, Crater Flat, Nevada. *Geochim. et. Cosmochim. Acta* **66**, 487–506 (2002).
70. Wedepohl, K. H. The composition of the continental crust. *Geochim. et. cosmochim. Acta* **59**, 1217–1232 (1995).
71. Mischel, S. A., Mertz-Kraus, R., Jochum, K. P. & Scholz, D. TERMITE: An R script for fast reduction of laser ablation inductively coupled plasma mass spectrometry data and its application to trace element measurements. *Rapid Commun. Mass Spectrom.* **31**, 1079–1087 (2017).
72. Team, R. C. R. Core Team R.: a language and environment for statistical computing. *Foundation for Statistical Computing* (2020).
73. Sforna, M.-C. & Lugli, F. MapIT!: a simple and user-friendly MATLAB script to elaborate elemental distribution images from LA-ICP-MS data. *J. Anal. At. Spectrom.* **32**, 1035–1043 (2017).
74. Scholz, D., Hoffmann, D. L., Hellstrom, J. & Ramsey, C. B. A comparison of different methods for speleothem age modelling. *Quat. Geochronol.* **14**, 94–104 (2012).
75. Comas-Bru, L. et al. SISALv2: a comprehensive speleothem isotope database with multiple age–depth models. *Earth Syst. Sci. Data* **12**, 2579–2606 (2020).
76. Scholz, D. & Hoffmann, D. L. StalAge–An algorithm designed for construction of speleothem age models. *Quat. Geochronol.* **6**, 369–382 (2011).
77. Breitenbach, S. F. et al. Constructing proxy records from age models (COPRA). *Climate* **8**, 1765–1779 (2012).
78. York, D., Evensen, N. M., Martínez, M. L. & De Basabe Delgado, J. Unified equations for the slope, intercept, and standard errors of the best straight line. *Am. J. Phys.* **72**, 367–375 (2004).
79. Vermeesch, P. IsoplotR. A free and open toolbox for geochronology. *Geosci. Front.* **9**, 1479–1493 (2018).
80. Ludwig, K. Mathematical–statistical treatment of data and errors for 230Th/U geochronology. *Rev. Mineral. Geochem.* **52**, 631–656 (2003).
81. Hemming, S. R. Heinrich events: Massive late Pleistocene detritus layers of the North Atlantic and their global climate imprint. *Rev. Geophys.* **42** (2004).
82. Goni, M. F. S. & Harrison, S. P. Millennial-scale climate variability and vegetation changes during the Last Glacial: Concepts and terminology. *Quat. Sci. Rev.* **29**, 2823–2827 (2010).

Acknowledgements

Financial support for this project was provided by the Deutsche Forschungsgemeinschaft through grant SCHO 1274/14-1 and INST 247/889-1 FUGG to DS and WE 7074/1-1 to MW. We also acknowledge financial support from the Max Planck Graduate Center Mainz. The authors would like to thank Viktoria Blumrich for assistance with the measurement of the ^{230}Th/U-ages and Sebastian Breitenbach for helpful discussions regarding this manuscript and the project in general. We would also like to thank the Thüringer Landesamt für Umwelt, Bergbau und Naturschutz and the Thüringer Höhlenverein e.V. for supporting the project and providing access to the cave and speleothem samples.

Author contributions

D.S. designed the study. J.K. conducted the sampling, the chemical preparation for the solution ^{230}Th/U analysis and the measurement for solution ^{230}Th/U-dating. M.W. set up the LA ^{230}Th/U dating method, M.W. and J.K. conducted the measurements of the LA ^{230}Th/U ages, M.W. evaluated the data. Trace element measurements and evaluation were performed by J.K. and the trace element mapping was done by M.W. and

J.K., M.W. evaluated the data. The script for age modelling was developed and written by D.S., and J.K. constructed the age models. All authors contributed to the discussion and interpretation of the data, and the writing of the manuscript.

Funding
Open Access funding enabled and organized by Projekt DEAL.

Competing interests
The authors declare no competing interests.

Additional information
Supplementary information The online version contains supplementary material available at https://doi.org/10.1038/s43247-024-01863-0.

Correspondence and requests for materials should be addressed to Jennifer Klose.

Peer review information *Communications Earth & Environment* thanks the anonymous reviewers for their contribution to the peer review of this work. Primary Handling Editors: Yuan Shang and Carolina Ortiz Guerrero. [A peer review file is available].